ARMY RESEARCH LABORATORY

Modeling Effects of Crystalline Microstructure, Energy Storage Mechanisms, and Residual Volume Changes on Penetration Resistance of Precipitate-Hardened Aluminum Alloys

by John D. Clayton

ARL-RP-266 **August 2009**

A reprint from *Composites, Part B*, Vol. 40, pp. 443–450, 2009.

NOTICES

Disclaimers

The findings in this report are not to be construed as an official Department of the Army position unless so designated by other authorized documents.

Citation of manufacturer's or trade names does not constitute an official endorsement or approval of the use thereof.

Destroy this report when it is no longer needed. Do not return it to the originator.

Army Research Laboratory
Aberdeen Proving Ground, MD 21005-5066

ARL-RP-266 **August 2009**

Modeling Effects of Crystalline Microstructure, Energy Storage Mechanisms, and Residual Volume Changes on Penetration Resistance of Precipitate-Hardened Aluminum Alloys

John D. Clayton
Weapons and Materials Research Directorate, ARL

A reprint from *Composites, Part B*, Vol. 40, pp. 443–450, 2009.

REPORT DOCUMENTATION PAGE

Form Approved
OMB No. 0704-0188

1. REPORT DATE *(DD-MM-YYYY)*	2. REPORT TYPE	3. DATES COVERED (From - To)
August 2009	Reprint	January 2007–January 2009

4. TITLE AND SUBTITLE
Modeling Effects of Crystalline Microstructure, Energy Storage Mechanisms, and Residual Volume Changes on Penetration Resistance of Precipitate-Hardened Aluminum Alloys

5a. CONTRACT NUMBER

5b. GRANT NUMBER

5c. PROGRAM ELEMENT NUMBER

6. AUTHOR(S)
John D. Clayton

5d. PROJECT NUMBER
AH80

5e. TASK NUMBER

5f. WORK UNIT NUMBER

7. PERFORMING ORGANIZATION NAME(S) AND ADDRESS(ES)
U.S. Army Research Laboratory
ATTN: RDRL-WMT-D
Aberdeen Proving Ground, MD 21005-5066

8. PERFORMING ORGANIZATION REPORT NUMBER
ARL-RP-266

9. SPONSORING/MONITORING AGENCY NAME(S) AND ADDRESS(ES)

10. SPONSOR/MONITOR'S ACRONYM(S)

11. SPONSOR/MONITOR'S REPORT NUMBER(S)

12. DISTRIBUTION/AVAILABILITY STATEMENT
Approved for public release; distribution is unlimited.

13. SUPPLEMENTARY NOTES
A reprint from *Composites, Part B*, Vol. 40, pp. 443–450, 2009.

14. ABSTRACT
An anisotropic nonlinear crystal mechanics model is developed for a class of ductile aluminum alloys, with the intent of relating microscopic features and properties to performance of the alloys deformed at high strain rates that may arise during impact and blast events. A direct numerical simulation of dynamic tensile deformation of an aluminum polycrystal demonstrates a tendency for shear localization to occur in regions of the microstructure where the ratio of the rate of residual (i.e., stored) elastic energy to plastic dissipation is minimal. By coarse-graining predictions of the crystal plasticity framework using a Taylor averaging scheme, a macroscopic constitutive model is developed to investigate effects of microstructure on ballistic perforation resistance of plates of an Al–Cu–Mg–Ag alloy. Specific aspects of microstructure investigated include random and rolled cubic textures as well as stored elastic energy and residual volume changes associated with lattice defects, impurities, and inclusions such as second phases in the metal–matrix composite. Results suggest performance could be improved by tailoring microstructures to increase the shear yield strength and the ratio of residual elastic energy to dissipated heat.

15. SUBJECT TERMS
elasticity, plasticity, thermodynamics, aluminum, metal–matrix composite

16. SECURITY CLASSIFICATION OF:			17. LIMITATION OF ABSTRACT	18. NUMBER OF PAGES	19a. NAME OF RESPONSIBLE PERSON
a. REPORT	b. ABSTRACT	c. THIS PAGE			John D. Clayton
Unclassified	Unclassified	Unclassified	UU	14	19b. TELEPHONE NUMBER (*Include area code*) 410-278-6146

Composites: Part B 40 (2009) 443–450

Contents lists available at ScienceDirect

Composites: Part B

journal homepage: www.elsevier.com/locate/compositesb

Modeling effects of crystalline microstructure, energy storage mechanisms, and residual volume changes on penetration resistance of precipitate-hardened aluminum alloys

J.D. Clayton

Impact Physics, US Army Research Laboratory, APG, MD 21005-5066, USA

ARTICLE INFO

Article history:
Received 7 November 2008
Received in revised form 5 January 2009
Accepted 7 January 2009
Available online 7 May 2009

Keywords:
A. Metal–matrix composite
B. Impact behavior
B. Plastic deformation
C. Micro-mechanics

ABSTRACT

An anisotropic nonlinear crystal mechanics model is developed for a class of ductile aluminum alloys, with the intent of relating microscopic features and properties to performance of the alloys deformed at high strain rates that may arise during impact and blast events. A direct numerical simulation of dynamic tensile deformation of an aluminum polycrystal demonstrates a tendency for shear localization to occur in regions of the microstructure where the ratio of the rate of residual (i.e., stored) elastic energy to plastic dissipation is minimal. By coarse-graining predictions of the crystal plasticity framework using a Taylor averaging scheme, a macroscopic constitutive model is developed to investigate effects of microstructure on ballistic perforation resistance of plates of an Al–Cu–Mg–Ag alloy. Specific aspects of microstructure investigated include random and rolled cubic textures as well as stored elastic energy and residual volume changes associated with lattice defects, impurities, and inclusions such as second phases in the metal–matrix composite. Results suggest performance could be improved by tailoring microstructures to increase the shear yield strength and the ratio of residual elastic energy to dissipated heat.

Published by Elsevier Ltd.

1. Introduction

Aluminum alloys, as a result of their low mass density, high strength, and high ductility, are of technological interest for vehicular applications, including aircraft and land vehicles. The class of materials of present study consists of bulk Al grains (face centered cubic or FCC crystal structure) and other phases that emerge as a result of incorporation of secondary elements, either within grains or near grain boundaries. The material of interest here, Al 2139, consists primarily of elemental Al and contains smaller amounts of Cu, Mg, Ag, Mn, and trace amounts of Si and Fe [3]. The microstructure may influence mechanical properties in a number of ways. For example, orientations of individual grains affect elastic compliance and yield strength; second phases influence dislocation mechanisms, and hence strength, ductility, and energy of cold working; and precipitates segregated at grain boundaries affect fracture strength. In Al–Cu–Mg–Ag alloys one important secondary phase is the Ω phase, with chemical composition Al_2Cu and orthorhombic crystal structure, which can nucleate as thin plates on {1 1 1} planes and in fine distributions leads to creep resistance and superior strength [14]. A number of other microscopic heterogeneities are also possible, including the θ phase (tetragonal crystal structure, also of composition Al_2Cu); dispersoids of Mn; and at the single-atom scale, point defects such as interstitials and vacancies associated with impurities. Polycrystalline Al 2139 can thus be labeled a metal–matrix composite, with the matrix phase itself a composite mixture of anisotropic grains, and with possible secondary phases consisting of Ω, θ, and/or Mn.

An increased understanding of mechanisms affecting dynamic mechanical performance of aluminum alloys is sought. Relationships between composition, processing routes, microstructure, strength, and ductility are needed. One goal of the present work is to suggest promising paths to tailor the material at the scale of individual crystals and lattice defect distributions in order to improve performance.

In the present paper, a new constitutive model capturing deformation of individual anisotropic crystals with effects of precipitates and impurities is developed, as presented in Section 2. A unique feature of the model not included in previous work on metals [4–6] is explicit consideration of the residual elastic volume change resulting from the energy of local stress fields of lattice defects [28,12,35]. More precise values of thermoelastic properties not considered in Clayton [6] are also used here, following Thomas [32]. The model is implemented in a dynamic finite element code; a representative simulation of grain morphology presented in Section 3 indicates heterogeneous localized deformation resulting from spatial variations in properties within the microstructure. In Section 4, a new macroscopic model accounting for homogenized behavior of the polycrystalline metal–matrix composite is presented, capturing strain-dependent variations in stored energy of defects in the

E-mail address: jclayton@arl.army.mil

1359-8368/$ - see front matter Published by Elsevier Ltd.
doi:10.1016/j.compositesb.2009.01.009

balance of energy and residual volume changes in the equation of state. The coarse-grained model's parameters are obtained via calibration to results of the crystal plasticity model, which itself is too computationally intensive to enable large scale ballistic simulations. Instead, macroscopic finite element-smooth particle dynamic simulations incorporating the homogenized material behavior are used to provide quantitative assessments of possible benefits of texturing and amplification of energy storage mechanisms on ballistic performance, as discussed in Section 5. Such information may be useful to alloy developers seeking processing paths for engineered materials at nano- and microscales that offer optimal performance in structural applications.

2. Model for anisotropic crystal mechanics

The present treatment of geometrically nonlinear, single crystal elastoplasticity extends previous theory [4,5] to account for free energy accumulation associated with interactions between dislocations and precipitates or interstitials as well as residual elastic volume changes. Standard notations of modern continuum mechanics are used. Boldface type is used for vectors and tensors, and italic font is used for scalars. Juxtaposition of boldface quantities implies matrix multiplication. The summation convention applies over repeated indices. For simplicity, Cartesian coordinates are used throughout.

The local deformation gradient $\mathbf{F}$ satisfies

$$\mathbf{F} = \partial_{\mathbf{X}}\varphi = \mathbf{F}^{\mathbf{E}}\mathbf{F}^{\theta}\bar{J}^{1/3}\mathbf{F}^{\mathbf{P}}, \tag{1}$$

where $\mathbf{X}$ are material coordinates, $\mathbf{x} = \varphi(\mathbf{X}, t)$ are spatial coordinates depending on time t, $\mathbf{F}^{\mathbf{E}}$ accounts for mechanical elastic deformation and rigid body rotation, $\mathbf{F}^{\theta}$ accounts for thermal expansion or contraction, and $\mathbf{F}^{\mathbf{P}}$ accounts for dislocation glide. The scalar $\bar{J}$ accounts for residual elastic volume changes associated with nonlinear elastic behavior and eigenstresses of defects [28,12]. The spatial velocity gradient following from (1) is

$$\mathbf{L} = \partial_{\mathbf{x}}\dot{\mathbf{x}} = \dot{\mathbf{F}}^{\mathbf{E}}\mathbf{F}^{\mathbf{E}-1} + \alpha_T\dot{\theta}\mathbf{1} + (1/3)\dot{\bar{J}}\bar{J}^{-1}\mathbf{1} + \mathbf{F}^{\mathbf{E}}\mathbf{F}^{\theta}\mathbf{L}^{\mathbf{P}}\mathbf{F}^{\theta-1}\mathbf{F}^{\mathbf{E}-1}, \tag{2}$$

where the superposed dot and -1 denote a material time derivative and matrix inversion. For cubic lattices, thermal deformation is isotropic. The coefficient of thermal expansion α_T may depend on temperature θ, and $\mathbf{1}$ is the unit tensor. Deviatoric plastic deformation satisfies the usual rate kinematics

$$\mathbf{L}^{\mathbf{P}} = \dot{\mathbf{F}}^{\mathbf{P}}\mathbf{F}^{\mathbf{P}-1} = \sum_{\alpha=1}^{n}\dot{\gamma}^{(\alpha)}\mathbf{s}_0^{(\alpha)} \otimes \mathbf{m}_0^{(\alpha)}, \tag{3}$$

where $\mathbf{s}_0^{(\alpha)}$ and $\mathbf{m}_0^{(\alpha)}$ denote the reference slip director and slip plane normal for glide system α, with n the total number of systems, and $\dot{\gamma}^{(\alpha)}$ is the shearing rate on system α. Slip directors and plane normals are mapped from the reference to deformed configuration via the thermoelastic deformation as follows:

$$\mathbf{s}^{(\alpha)} = \mathbf{F}^{\mathbf{E}}\mathbf{F}^{\theta}\bar{J}^{1/3}\mathbf{s}_0^{(\alpha)}, \quad \mathbf{m}^{(\alpha)} = \mathbf{m}_0^{(\alpha)}\bar{J}^{-1/3}\mathbf{F}^{\theta-1}\mathbf{F}^{\mathbf{E}-1}. \tag{4}$$

In FCC crystals, usual Burgers vectors for mobile dislocations are of the type $a/2\langle 1\,1\,0\rangle$, with magnitude $b = \sqrt[-1]{2}a$, where a is the lattice parameter of the conventional unit cell. Glide planes are of orientation $\{1\,1\,1\}$, leading to 12 independent slip systems of type $\langle 1\,\bar{1}\,0\rangle\{1\,1\,1\}$.

The Helmholtz free energy per unit mass is denoted by ψ. The specific free energy density of the crystal is written

$$\tilde{\rho}\psi = \underbrace{\frac{1}{2}E^E_{\alpha\beta}\mathbb{C}^{\alpha\beta\chi\delta}E^E_{\chi\delta}}_{\text{second-order elasticity}} + \underbrace{\frac{1}{6}E^E_{\alpha\beta}\mathbb{C}^{\alpha\beta\chi\delta\varepsilon\phi}E^E_{\chi\delta}E^E_{\varepsilon\phi}}_{\text{third-order elasticity}} + \underbrace{\frac{1}{2}\kappa\Omega\mu\xi^2}_{\text{lattice defects}} - \underbrace{\tilde{\rho}\hat{c}\theta\log(\theta/\theta_0)}_{\text{thermal energy}}, \tag{5}$$

where on the left, $\tilde{\rho} = J^E\rho$ is the mass density of the elastically unloaded material, ρ is the mass density of the deformed material, and $J^E = \det\mathbf{F}^{\mathbf{E}}$. Components of elastic strain are $2E^E_{\alpha\beta} = F^{Ea.}_{\alpha}\delta_{ab}F^{Eb.}_{\beta} - \delta_{\alpha\beta}$, with Kronecker's delta denoted by δ, and summation is invoked over repeated Greek and lower-case Roman indices. Second- and third-order elastic coefficients, $\mathbb{C}^{\alpha\beta\chi\delta}$ and $\mathbb{C}^{\alpha\beta\chi\delta\varepsilon\phi}$, may generally depend on temperature, as may the effective shear modulus μ. Aluminum single crystals exhibit three independent second-order elastic coefficients and six independent third-order coefficients [32]. Also in (5), κ and Ω are dimensionless scalars, $\hat{c}$ is the specific heat per unit mass, and θ_0 is a scalar temperature at which the thermal energy vanishes. The scalar internal state variable ξ is defined by

$$\xi = b\sqrt{\rho_T}, \tag{6}$$

where ρ_T is the total line length per unit volume of dislocations, in general both mobile and immobile, associated with stored energy of cold working [26] and strain hardening during plastic flow. Thermodynamic arguments [4,5] lead to the stress–strain relations

$$S^{\alpha\beta} = J^E F^{E-1\alpha}_{.a}\sigma^{ab}F^{E-1\beta}_{.b} = \tilde{\rho}\frac{\partial\psi}{\partial E^E_{\alpha\beta}} = \mathbb{C}^{\alpha\beta\chi\delta}E^E_{\chi\delta} + \frac{1}{2}\mathbb{C}^{\alpha\beta\chi\delta\varepsilon\phi}E^E_{\chi\delta}E^E_{\varepsilon\phi}, \tag{7}$$

with $\mathbf{S}$ the elastic second Piola–Kirchhoff stress and $\boldsymbol{\sigma}$ the Cauchy stress. The local energy balance in the spatial configuration is

$$\underbrace{\rho\hat{c}\dot{\theta}}_{\text{temperature change}} = \underbrace{\sum_{\alpha=1}^{n}\tau^{(\alpha)}\dot{\gamma}^{(\alpha)}}_{\text{dissipation from slip}} - \underbrace{p\dot{\bar{J}}\bar{J}^{-1}}_{\text{residual volume changes}} - \underbrace{\rho\left(\frac{\partial\psi}{\partial\xi} - \theta\frac{\partial\,\psi}{\partial\theta\partial\xi}\right)\dot{\xi}}_{\text{energy of lattice defects}} + \underbrace{\theta\left(\frac{\rho\partial\,\psi}{\partial\theta\partial\mathbf{E}^{\mathbf{E}}} - \frac{\alpha_T\,\partial p}{\partial\mathbf{E}^{\mathbf{E}}}\right):\dot{\mathbf{E}}^{\mathbf{E}}}_{\text{thermoelastic coupling}} - \underbrace{\partial_{\mathbf{x}}\cdot\mathbf{q}}_{\text{heat conduction}}, \tag{8}$$

where $\tau^{(\alpha)} = \boldsymbol{\sigma} : \mathbf{s}^{(\alpha)} \otimes \mathbf{m}^{(\alpha)}$ is the resolved shear stress on system α, p is the Cauchy pressure, and $\mathbf{q}$ is the heat flux satisfying

$$\mathbf{q} = -k\partial_{\mathbf{x}}\theta, \tag{9}$$

where k is the scalar thermal conductivity. Symbols $\cdot$ and : in (8) denote contraction over one and two sets of indices, respectively.

Following the generic Arrhenius form for thermally activated kinetics,

$$\dot{\gamma}^{(\alpha)} = \dot{\gamma}_0\exp[-G^{(\alpha)}/(k_B\theta)], \tag{10}$$

where $\dot{\gamma}_0$ is a constant with dimensions of $1/t$, k_B is Boltzmann's constant, and $G^{(\alpha)}$ is the Gibbs activation energy that depends upon the state variables [4,5,33]:

$$G^{(\alpha)} = -mk_B\theta[\log(\tilde{\tau}^{(\alpha)}/g_0^{(\alpha)}) - r\log(\theta/\theta_0)]. \tag{11}$$

Here m and r are dimensionless parameters denoting rate and temperature sensitivity, respectively, and $\tilde{\tau}^{(\alpha)} = J^E\tau^{(\alpha)}$. The larger the value of m, the less rate sensitive the flow stress. A negative value of r leads to thermal softening from increased dislocation mobility with increasing temperature. The transient slip resistance $g_0^{(\alpha)} = g_y^{(\alpha)} + \Delta g^{(\alpha)}$ arises from the sum of (i) the initial distribution of defects, lattice friction, and viscous, phonon, and electron drag via constant $g_y^{(\alpha)}$; and (ii) evolving barriers to slip such as accumulated forest dislocations via state variable-dependent contribution $\Delta g^{(\alpha)}(\xi, t)$. The evolution of slip resistance at reference temperature θ_0 is dictated by a hardening-minus-dynamic-recovery relation:

$$\dot{g}_0^{(\alpha)} = A\sum_{\beta=1}^{n}q_\beta^\alpha|\dot{\gamma}^{(\beta)}| - Bg_0^{(\alpha)}\sum_{\beta=1}^{n}|\dot{\gamma}^{(\beta)}|, \quad q_\beta^\alpha = \delta_\beta^\alpha + q(1-\delta_\beta^\alpha), \tag{12}$$

where q is the latent hardening ratio equal to unity in what follows [22], such that all n systems harden equally. In (12), A and B are constants. The constant $g_y^{(\alpha)}$ is independent of strain rate and temperature and reflects the initial yield stress at $\theta = \theta_0$. Thus, $\dot{g}_0^{(\alpha)} = d(\Delta g^{(\alpha)})/dt$, where $\dot{g}_0^{(\alpha)}$ is evaluated according to (12). Possible influences of rate and temperature on the evolution of hardness $g_0^{(\alpha)}$ are apparent upon substitution of the slip rates from (10) and (11) into (12). The zero subscript on the notation $g_0^{(\alpha)}$ is not necessary, but it is used for consistency with previous work [4,5,33]. The origin of this subscript follows from the argument that at $\theta = \theta_0$, temperature does not affect the apparent yield stress entering the flow rule (10) resulting from the form of the activation energy in (11).

The following relationship between hardening and the accumulated dislocation line density is used [29]:

$$\Delta g^{(\alpha)} = \hat{\alpha}\mu b\sqrt{\rho_T}. \tag{13}$$

Scalar proportionality factor $\hat{\alpha}$ accounts for dislocation interactions. The residual elastic energy per unit volume from dislocations E_S is estimated as

$$E_S = \frac{1}{2}\kappa\Omega\mu\xi^2 = \frac{1}{2}\kappa\Omega\mu b^2\rho_T = \left[\frac{\mu b^2}{4\pi}\log\frac{R}{R_C}\right]\Omega\rho_T. \tag{14}$$

The first two equalities in (14) offer a phenomenological representation of the stored energy of the local stress fields of dislocations. Such a linear relationship between the scalar dislocation density and stored energy has been described elsewhere [23,4,5]; in this relationship, the product $\kappa\Omega$ is simply a proportionality constant to be calibrated from experimental measurements on stored energy of cold work [26]. The term following the final equality includes the well-known logarithmic energy per unit length of a screw dislocation in an isotropic body of infinite extent [13]. Multiplying this energy per unit length by the product of the line length per unit volume of dislocations and the scaling factor Ω then gives the total energy per unit volume. The relationship $R/R_C = \exp(2\pi\kappa)$ is obtained by straightforward algebra. For straight, non-interacting screw dislocation lines, a typical estimate is $\kappa\Omega \sim 2$ [13]. Contributions of κ to deviations from this approximate value (i.e., $\kappa\Omega \neq 2$) account for elastic anisotropy, core effects, elastic nonlinearity, edge and mixed character of dislocations, and dislocation line curvature. The parameter Ω is described in more detail below. The volume change associated with the residual elastic energy of (14) is [28,12]

$$\bar{J} = 1 + \mu^{-1}(\partial\mu/\partial p - \mu/K)E_S = 1 + (\kappa\Omega b^2\rho_T/2)(\partial\mu/\partial p - \mu/K), \tag{15}$$

where for a cubic crystal with second-order constants $\mathbb{C}_{11}, \mathbb{C}_{12}$, and $\mathbb{C}_{44}$, the appropriate bulk and shear moduli K and μ satisfy $3K = \mathbb{C}_{11} + 2\mathbb{C}_{12}$ and $2\mu^2 = \mathbb{C}_{44}(\mathbb{C}_{11} - \mathbb{C}_{12})$. The elastic coefficients and the pressure derivative of the shear modulus in (15) are all measured at the stress-free reference state. The Taylor–Quinney factor β dictating plastic work-to-heat conversion in adiabatic processes [10,31,26] is defined as

$$\beta = \left(\sum_{\alpha=1}^{n}\tau^{(\alpha)}\dot{\gamma}^{(\alpha)} - \rho(\partial\psi/\partial\xi - \theta\partial^2\psi/\partial\theta\partial\xi)\dot{\xi}\right)\left(\sum_{\alpha=1}^{n}\tau^{(\alpha)}\dot{\gamma}^{(\alpha)}\right)^{-1}, \tag{16}$$

such that $1-\beta$ is the ratio of the rate of stored residual elastic energy to dissipation resulting from dislocation glide. Manipulating (6) followed by time differentiation gives

$$\xi = \frac{\tilde{\rho}\partial\psi/\partial\xi}{\kappa\mu\Omega} = \frac{1}{\hat{\alpha}\mu n}\sum_{\alpha=1}^{n}\Delta g^{(\alpha)}, \quad \dot{\xi} = b\frac{\dot{\rho}_T}{2\sqrt{\rho_T}} \approx \frac{1}{\hat{\alpha}\mu n}\sum_{\alpha=1}^{n}\dot{g}_0^{(\alpha)}. \tag{17}$$

Furthermore, from (5) and (13),

$$\tilde{\rho}\theta\frac{\partial^2\psi}{\partial\theta\partial\xi} = \frac{\kappa\Omega\theta}{\hat{\alpha}\mu n}\frac{\partial\mu}{\partial\theta}\sum_{\alpha=1}^{n}\Delta g^{(\alpha)}, \quad \rho_T = \left[\frac{1}{\hat{\alpha}\mu n b}\sum_{\alpha=1}^{n}\Delta g^{(\alpha)}\right]^2. \tag{18}$$

Substituting (17) and (18) into (16) then yields

$$\beta = 1 - \kappa\Omega\left(\mu + \theta\frac{\partial\mu}{\partial\theta}\right)\left[\sum_{\alpha=1}^{n}\Delta g^{(\alpha)}\sum_{\alpha=1}^{n}\dot{g}_0^{(\alpha)}\right]\left[(\hat{\alpha}\mu n)^2\sum_{\alpha=1}^{n}\tilde{\tau}^{(\alpha)}\dot{\gamma}^{(\alpha)}\right]^{-1}. \tag{19}$$

As is clear from (8) and (19), when κ is held fixed, values of $\Omega > 1$ amplify the stored energy associated with internal variable ξ and equivalently, the residual elastic energy engendered by microscopic stress fields arising from the dislocation density ρ_T. Such amplification would manifest physically in Al–Cu–Mg–Ag alloys from the presence of second-phase particles of Ω, θ, or Mn that can act as local stress risers [2] or barriers to dislocation motion. The increase in stored energy would be attributed to both the elastic energy of the deforming second phases and misfit stresses [17], as well as the elastic interaction energies of dislocations that may build up at grain and phase boundaries. While κ accounts for the self-energy of dislocations as discussed following (14), Ω accounts for interaction energies of dislocations with second phases, point defects or impurities, and other dislocations. If the dislocation density vanishes in a reference configuration of minimum free energy (e.g., a perfect lattice) then the product $\kappa\Omega$ must be positive to ensure that the free energy (5) increases with increasing defect content. Values $\Omega < 1$ are permissible and would reduce the stored energy associated with lattice defects when κ is held fixed.

Parameters entering the single crystal model, many specific to alloy Al 2139, are compiled in Table 1. Because in applications of present interest, slip takes place before large deviatoric elastic strains can arise, third-order elastic constants in (5) are represented by the simple form [5,7]

$$\overline{\mathbb{C}}^{\alpha\beta\chi\delta\varepsilon\phi} = -2K_1\delta^{\alpha\beta}\delta^{\chi\delta}\delta^{\varepsilon\phi}, \tag{20}$$

where $K_1 > 0$ accounts for the increase in apparent bulk modulus with increasing pressure. Elastic constants and their pressure and temperature derivatives are obtained from Thomas [32]. The remaining parameters in Table 1 are obtained from the plasticity literature or calibration to experimental data for Al 2139 [3], with a random texture as explained in Clayton [6]. The large value of m implies rate insensitivity. A range of values of $1 \leqslant \Omega \leqslant 8$ is considered to investigate effects of stored energy on the thermomechanical response, as explained in detail in Section 4.

3. Mesoscale simulation

A direct numerical simulation of individual anisotropic grains is performed first to provide insight into the high rate mechanical response of the alloy at the scale of the microstructure.

Table 1
Parameters for crystal model.

Parameter	Value	Parameter	Value
$\mathbb{C}_{11}$ [GPa]	108	α_T [1/K]	$2.3(10)^{-5} + 1.7(10)^{-8}\Delta\theta$
$\mathbb{C}_{12}$ [GPa]	60.4	$\hat{c}$ [J/kgK]	$900 + 0.466\Delta\theta$
$\mathbb{C}_{44}$ [GPa]	28.3	$g_y^{(\alpha)}$ [GPa]	0.155
$\partial\mathbb{C}_{11}/\partial\theta$ [MPa/K]	−35.1	q	1.0
$\partial\mathbb{C}_{12}/\partial\theta$ [MPa/K]	−6.7	$\hat{\alpha}$	0.3
$\partial\mathbb{C}_{44}/\partial\theta$ [MPa/K]	−14.5	b [nm]	0.286
$\partial\mu/\partial p$	1.75	$\dot{\gamma}_0$ [1/s]	0.001
K_1 [GPa]	36.7	m	50
ρ_0 [kg/m^3]	2700	n	12
κ	10	A [GPa]	0.48
θ_0 [K]	300	B	1.5
θ_1 [K]	934	r	−1.1
k [W/mK]	237	Ω	1.0, 4.0, 8.0

Representative results are shown in Fig. 1. Properties are chosen to correspond to an Al 2139 alloy of the type described in Table 1, with $\Omega = 1$. As will be demonstrated later in Section 4, this leads to an average value of the heat dissipation fraction β on the order of 0.90–0.95 when considered over a range of strains from zero to unity. Such a prediction is in general agreement with experimental observations of Farren and Taylor [10], Havner [11], and references therein, who noted for commercially pure polycrystalline aluminum an average value of $\beta \sim 0.93$. In the present model, effects of inclusions and precipitates are treated implicitly by the choice of material parameters, meaning that the second phase particles are not modeled explicitly. In the present context, the impurities are too small to resolve efficiently using continuum finite elements: Mn dispersoids are of diameter $0.1 - 0.5$ μm [3], and Ω platelets are of thickness less than 0.1 μm [14]. The size of the computational domain is 1 mm × 1 mm, consisting of 100 grains of an average size of 100 μm, with a random initial texture. Polygonal grain shapes are created using a Voronoi technique [9,25] with selective mesh refinement in the vicinity of grain boundaries [4,5]. The finite element method with explicit dynamics and heat conduction is used in the calculations, as described in [4,5].

The boundary conditions are plane strain, with an applied stretch in the vertical direction resulting from a velocity of 10 m/s applied to the upper surface and the bottom surface fixed in the vertical direction. An initial velocity gradient component in the direction of stretch of magnitude $10^4/\mathrm{s}$ is assigned throughout the domain to minimize inertial effects. These boundary conditions provide an average applied tensile strain rate of $10^4/\mathrm{s}$. Plane strain boundary conditions are used for the two-dimensional simulations because they are deemed more representative (than plane stress, for example) of conditions experienced by a polycrystalline volume element embedded within a much larger sample of material [38,4]. Special force boundary conditions applied along the lateral edges constrain these edges to remain vertically straight and parallel, yet free to contract inwardly due to the Poisson effect as the mesh undergoes tensile stretch. The lateral edges are free of shear traction. A uniform acceleration in the direction of contraction is assigned to all nodes of a lateral edge, with the value of this nodal acceleration computed for each explicit time step by dividing the total reaction force along the edge by the total mass of the nodes comprising that edge. A similar methodology was used in explicit simulations of polycrystalline microstructures by Zhou et al. [38] for imposing periodic shear deformations by averaging forces over periodic pairs of nodes. The boundary constraints are intended to instill the mesh with a global deformation mode that could be representative of a polycrystalline volume element embedded within a much larger sample. For example, spatial coordinates of the boundaries move in an affine manner according to $\mathbf{x} = \bar{\mathbf{F}}\mathbf{X}$, where components $\bar{F}^1_{\ 1}$ and $\bar{F}^2_{\ 2}$ measure, respectively, the average lateral contraction and average applied stretch, $\bar{F}^3_{\ 3} = 1$ in plane strain,

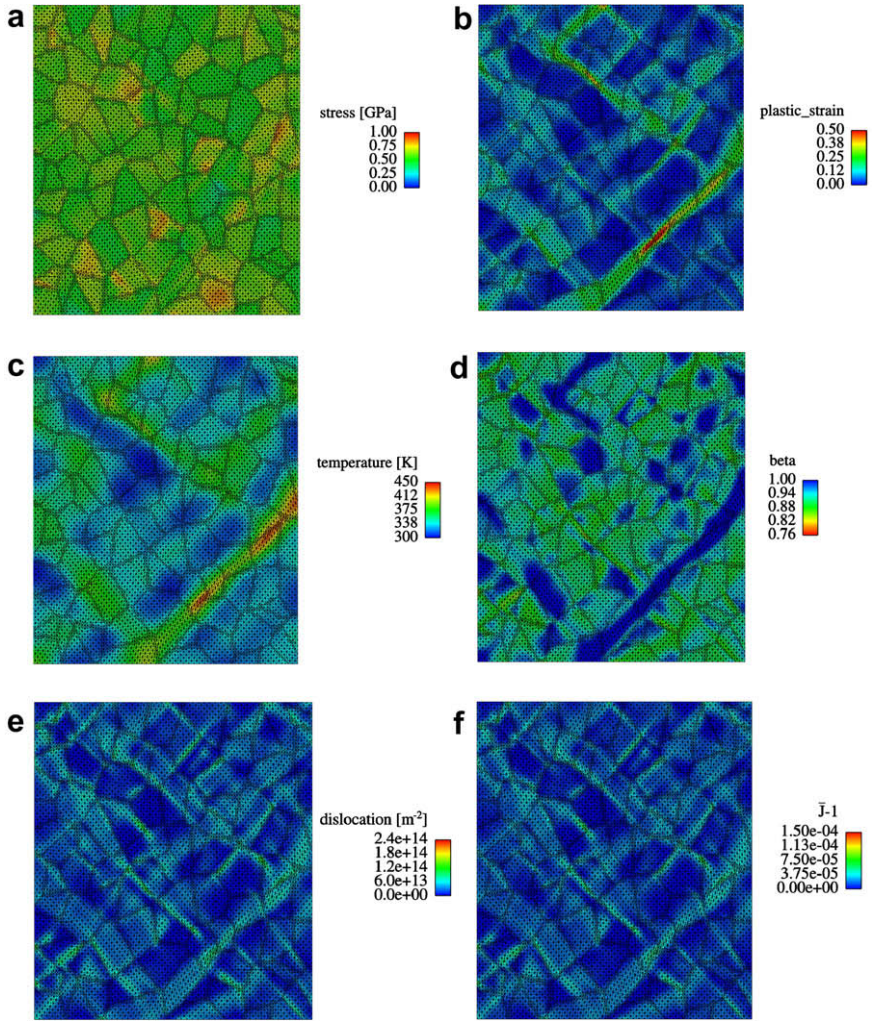

Fig. 1. Simulated Al polycrystal with random grain orientations at applied tensile strain of 8%: (a) effective stress, (b) effective plastic strain, (c) temperature, (d) dissipation fraction, (e) dislocation density, (f) residual volume change.

and $\bar{F}^a_A = 0$ for $a \neq A$. These affine displacement conditions are analogous to a macroscopic deformation gradient $\bar{\mathbf{F}}$ imposed on a single linear finite element containing a representative volume of microstructure. Although the assumption of plane strain may inhibit the formation of localized deformation modes such as shear banding and necking, the plane strain condition has been used extensively by a number of authors to study shear localization phenomena in the context of crystal plasticity or viscoplasticity [21,38,1]. The constraint imposed on the lateral edges of the mesh in the present work may also inhibit shear localization; for example, necking of the sample would be possible if the lateral edges were completely free of traction. Thus, the combination of plane strain and linear displacement conditions used here is expected to provide a stiffer response than other possible choices of boundary conditions such as plane stress or applied traction conditions (e.g., null tractions along the lateral edges). The boundary conditions used here are sufficient to provide some insight into the physics of shear localization in a representative polycrystalline sample via examination of the field variables (Fig. 1), but a more thorough investigation, reserved for future work, would also consider of other kinds of boundary conditions. Three-dimensional elastic and plastic deformations are permissible, with the full number of potentially active slip systems, so long as total deformation remains planar, as assumed in a number of previous works [8,4,5,33]. A uniform initial temperature of 300 K is assigned along with null heat flux conditions normal to the external boundary. Several mesh densities were investigated, and to the strain levels shown in Fig. 1, the results are insensitive to the mesh size.

Results in Fig. 1 correspond to an 8% applied strain, that is, $t = 8$ μs. Shown in Fig. 1(a) is the scalar effective stress, found by $\bar{\sigma} = ((3/2)\boldsymbol{\sigma}' : \boldsymbol{\sigma}')^{1/2}$, with $\boldsymbol{\sigma}'$ the deviatoric part of the Cauchy stress. Most grains support stresses on order of 0.5 GPa, but owing to orientation and elastic–plastic anisotropy, some grains are stiffer or more compliant than others. Shown in Fig. 1(b) is the cumulative effective plastic strain found by $\varepsilon_P = \int ((2/3)\mathbf{D}^{\mathbf{P}} : \mathbf{D}^{\mathbf{P}})^{1/2} dt$, where $\mathbf{D}^{\mathbf{P}}$ is the symmetric part of $\mathbf{L}^{\mathbf{P}}$ in (3). Several bands of localized deformation are apparent, most notably that on the lower right side of the domain, in which the plastic strain approaches 0.5. As is clear from Fig. 1(c), regions of intense strain correlate with regions of greatest temperature rise, with temperatures on the order of 450K attained in portions of the band. As shown in Fig. 1(d), the dissipation fraction β correlates positively with temperature rise and plastic strain localization. Note the inverse color scale used in Fig. 1(d), such that red areas correspond to an increased rate of energy storage. This correlation is obvious from consideration of the energy balance and thermal softening kinetics in (11): larger values of β lead to larger amounts of energy converted to temperature rise, which in turn leads to increased thermal softening. Reasons for relatively large local values $\beta \sim 1$ in the vicinity of regions of intense plastic strain include (i) local dislocation content approaching saturation such that rates of hardening and energy storage are minimal; (ii) large magnitudes of slip rates contributing to the denominator in (16); and (iii) large temperature rise contributing to the product $\theta \partial \mu / \partial \theta < 0$ in (19). Shear localization due to adiabatic heat generation and thermal softening in ductile metals can occur similarly in compression, shear, and mixed-mode loading [36]. Shown in Fig. 1(e) is the dislocation density associated with cumulative hardening in (13), while shown in Fig. 1(f) is the residual elastic volume change $\bar{J} - 1$ from (15). Dislocation densities of the same order of magnitude have been predicted elsewhere [24,25] in grain-scale crystal plasticity simulations of FCC metals. The volume changes predicted here are small and do not significantly affect the pressure (e.g., $\Delta p \approx 1.5 \times 10^{-4} K \approx 12$ MPa), and occur in regions where the dislocation density is highest. According to (15), the dislocation density and the residual volume change are linearly related, with $(\bar{J} - 1)/\rho_T$ varying with temperature as a result of the affect of temperature on the elastic moduli.

In summary, the results in Fig. 1 demonstrate positive correlations among temperature rise, plastic strain, and the heat dissipation fraction β. Increases in parameter Ω, via processing steps to increase the capacity for stored energy of mechanical working, would reduce β, heat conversion, and the tendency for localization of plastic deformation. Texturing could conceivably increase stress-carrying capacity, for example, via inclusion of a higher proportion of the stiffer grains evident in Fig. 1(a). A more extensive study would consider a large number of microstructure morphologies, grain orientation sets, and loading rates; however, the present mesoscale simulation is sufficient to demonstrate mechanisms to be exploited in what follows. Specifically, two mechanisms for possible performance enhancement – grain orientation and energy storage – are considered.

4. Coarse-grained macroscopic model

Homogenized results of a number of polycrystal calculations are used to provide parameters for a macroscopic plasticity model used in impact simulations. Polycrystalline aggregates consisting of 300 crystals are subjected to uniform shearing at a constant rate via $F^1_3 = 1 + \dot{\gamma} t$, where the shear strain is $\gamma = \dot{\gamma} t$. The shear boundary conditions at an applied rate of $\dot{\gamma} = 10^4/\text{s}$ are those deemed most crucial in a ballistic perforation event [27]. Each grain in the aggregate is sheared adiabatically under the same total deformation gradient [30,4], and each grain has the same volume. In the polycrystal calculations, two initial textures are considered: random and cubic. The random texture is representative of the simulation in Section 3 and results in Fig. 1, while the cubic texture can be obtained in a ductile plate by rolling [34]. In a previous work [6], a number of different rolled textures [34] were considered, with cubic found to give the greatest increase in the shear stress component thought to provide the primary resistance to plug formation [19,27]. For the random texture, each grain is assigned an independent set of three Euler angles with a random number generator, providing for isotropic average behavior. To obtain shear strength properties appropriate for a plate with a cubic texture subject to perforation, grains are all aligned with one cube axis parallel to the normal direction of the Al plate, that is, parallel to x^3, the direction of perforation. The other two cube axes are distributed randomly among the grains in the plane of the plate, the $x^1 - x^2$ plane. This provides for transversely isotropic symmetry, and allows for an average resistance of the plate to perforation by a cylindrical projectile that would arise from a true cubic texture with the three cube axes aligned with the normal, transverse, and rolling directions, respectively [6]. For each initial texture (i.e., random or cubic), values of $\Omega = 1, 4,$ or 8 are also considered, to investigate possible strengthening effects from energy storage.

The volume-averaged shear stress of the aggregate, $\bar{\tau} = V^{-1} \int \sigma^{13} dV$, is shown in Fig. 2. Each grain can support a different individual shear stress as a result of its particular lattice orientation. Cubic texturing provides a $\sim 25\%$ increase in peak shear strength over aggregates with random texture. Increases in energy storage factor Ω result in a slight increase in shear strength, for example for random grains at $\gamma = 0.4, \bar{\tau} = 0.446$ GPa for $\Omega = 1$ compared to $\bar{\tau} = 0.471$ GPa for $\Omega = 8$. The strength difference arises from the greater heat generated for $\Omega = 1$, leading to more thermal softening relative to the prediction for $\Omega = 8$. Since all grains are assigned the same deformation, no representation of localization is included in the results of Fig. 2 that would enhance the strength distinction afforded by different values of Ω.

The average dissipation fraction $\bar{\beta} = V^{-1} \int \beta dV$ is shown in Fig. 3. Each grain can provide a different value of the local dissipation fraction (i.e., the integrand) as a result of its own orientation. In all cases, this quantity decreases initially in conjunction with

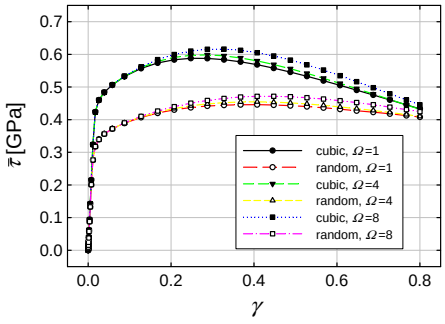

Fig. 2. Average shear stress versus shear strain for Al 2139 polycrystals of various microstructures.

work hardening and dislocation multiplication, then increases asymptotically towards unity at large strains as the dislocation content saturates [36,4]. Small differences in the dissipation fraction arise between random and cubic textures. Large differences arise from the choice of Ω, as expected from (19). As noted previously, commercially pure polycrystalline Al exhibits an average cumulative value of $\bar{\beta} \sim 0.93$ [11]. Slightly higher values, e.g. ~ 0.95 at strain levels approaching 50%, have been noted for pure aluminum single crystals [10]. The energy storage is presumably greater in polycrystals because of concentrated residual elastic energy near grain boundaries and triple points, as has been predicted in mesoscale simulations of FCC polycrystals [8]. Also shown in Fig. 3 are high-rate experimental results from Rosakis et al. [26] of rate-insensitive alloy Al 2024-T351, where the compressive plastic strains ε_P reported in that work are converted to equivalent shear strains using $\gamma \approx \sqrt{3}\varepsilon_P$. The adjustable parameter Ω dictates the ratio of the rate stored residual elastic energy to inelastic stress power, as is clear from Fig. 3. The larger the value of Ω, the greater the stored energy. Experimental data on $\bar{\beta}$ is not available for Al 2139 which is also fairly rate insensitive ([6] and references therein), but the results in Fig. 3 demonstrate that a physically reasonable range of $\bar{\beta}$ is provided by $1 \leqslant \Omega \leqslant 8$. The dissipation fraction of Al 2024-T351 would seem to correspond to Ω between 4 and 8, while pure Al would correspond to $\Omega \approx 1$. On the other hand, for alloys of different composition or processing routes, Ω may deviate from these values. Differences in Ω may arise among different alloys because of variations in composition and microstructure. Quantitative expressions relating Ω to precipitate sizes and volume fractions, impurity concentrations, and dislocation distributions remain to be determined by careful microscopic experiments and numerical simulations at the scale of discrete dislocation dynamics or molecular dynamics.

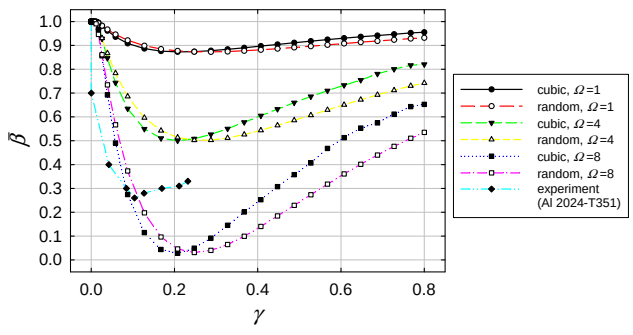

Fig. 3. Average heat dissipation fraction versus shear strain for Al 2139 polycrystals of various microstructures; experimental data points estimated from Rosakis et al. [26].

The plasticity component of the macroscopic model used here to represent Al 2139 in ballistic simulations follows from Zerilli and Armstrong [37]. For FCC metals such as Al, the yield surface in terms of deviatoric strength is

$$\bar{\sigma} = C_0 + C_2\bar{\varepsilon}_P^N \exp(-C_3\theta + C_4\theta \log \dot{\varepsilon}), \tag{21}$$

where $\dot{\varepsilon} = ((2/3)\mathbf{D} : \mathbf{D})^{1/2}$ is the effective total strain rate and $\mathbf{D}$ is the symmetric part of the total velocity gradient $\mathbf{L}$. Symbols C_0, C_2, C_3, C_4, and N denote fitting parameters, and $\overline{G}$ is the macroscopic shear modulus. Values corresponding to the Al alloy of present interest with different textures are listed in Table 2; specifically, $C_4 = 0$ implies rate insensitivity, and C_2 is higher for the cubic texture than the random texture, leading to the increased flow stress of the former evident in Fig. 2. These parameters are obtained by fitting (21) to the results of the polycrystal simulations of Fig. 2, again assuming adiabatic conditions. Note that the material is treated in the coarse scale model as isotropic, a rigorous assertion only for Al plates of the random texture. The cubic orientation would afford transverse isotropy, as discussed above. Thus, the normal strength of cubic-textured plate in the x^3-direction and the shear stresses σ^{12} and σ^{23} may be over- or underestimated by the assumption of isotropy. However, the predictions of dynamic perforation will be accurate so long as the primary resistance to plugging is the shear stress $\tau = \sigma^{13}$ tangential to the penetration direction [19,27]. Also shown in Table 2 are properties for iron used to model the projectile in impact simulations that are described in Section 5. The dynamic yield stress of iron is given by the BCC Zerilli–Armstrong model [37]:

$$\bar{\sigma} = C_0 + C_1 \exp(-C_3\theta + C_4\theta \log \dot{\varepsilon}) + C_5\bar{\varepsilon}_P^N, \tag{22}$$

with C_1 and C_5 additional parameters. The local macroscopic energy balance, i.e. the analog of (8) under adiabatic conditions, is

$$\rho\hat{c}\dot{\theta} = \bar{\beta}\boldsymbol{\sigma} : \mathbf{D}^{\mathbf{P}} + \varsigma(\rho, \theta, \bar{J}), \tag{23}$$

where ς accounts for effects of the equation of state of the material that relates mass density, temperature, and defect content to hydrostatic pressure. The effect of residual elastic volume changes in (15) is captured in a modified Mie–Gruniesen equation of state as

$$p = (\overline{K}\bar{\mu} + \overline{K}_2\bar{\mu}^2 + \overline{K}_3\bar{\mu}^3)(1 - \Gamma\bar{\mu}/2) + \Gamma\rho_0\hat{c}\Delta\theta(1 + \bar{\mu}), \tag{24}$$

where $\overline{K}, \overline{K}_2$, and $\overline{K}_3$ are dilatational elastic constants, Γ is Gruniesen's parameter, and $\bar{\mu} = \bar{J}J^{-1} - 1$ measures recoverable elastic volume changes. The reference mass density is $\rho_0 = \rho J = \rho \det \mathbf{F}$. Library property values for aluminum [18] are used in (24) in the ballistic simulations that follow. In the macroscopic model the residual volume change is found by

$$\begin{aligned}\bar{J} &= 1 + (\bar{E}_S/\overline{G})(\partial\overline{G}/\partial p - \overline{G}/\overline{K}) \\ &= 1 + \overline{G}^{-1}(\partial\overline{G}/\partial p - \overline{G}/\overline{K}) \int (1 - \bar{\beta})J\boldsymbol{\sigma} : \mathbf{D}^{\mathbf{P}} dt.\end{aligned} \tag{25}$$

The integral in the final term of (25) is the cumulative macroscopic stored energy per unit reference volume $\bar{E}_S$, and $\overline{G}$ is the polycrystalline

Table 2
Parameters for coarse-scale plasticity model.

Parameter	Al 2139, random	Al 2139, cubic	Iron[1]
C_0 [GPa]	0.40	0.40	0.65
C_1 [GPa]	–	–	1.03
C_2 [GPa]	2.5	4.5	–
C_3 [1/K]	0.0045	0.0045	0.0070
C_4 [1/K]	0	0	$4.16(10)^{-4}$
C_5 [GPa]	–	–	0.27
N	0.30	0.30	0.29
$\overline{G}$ [GPa]	26.0	26.0	80.2

[1] Zerilli and Armstrong [37].

shear modulus listed in Table 2. The first relationship in (25) is recognizable as the macroscopic (polycrystalline) analog of the single crystal expression for residual volume change in the first of (15). The dissipation fraction $\bar{\beta}$ in (23) and (25) is treated as a polynomial function of the effective plastic strain:

$$\bar{\beta} = 1 + B_1\varepsilon_P + B_2\varepsilon_P^2 + B_3\varepsilon_P^3. \tag{26}$$

Values of B_1, B_2, and B_3 are calibrated to the results of polycrystal simulations of Fig. 3 and are listed in Table 3 for each microstructure. The projectile is assigned the same properties in all simulations, with the default value of $\bar{\beta} = 1$ and library equation-of-state parameters [15].

5. Terminal ballistics predictions

Twelve impact simulations are performed to demonstrate possible effects of initial texture and energy storage on perforation resistance of an Al–Cu–Mg–Ag plate. These include plates of one of six different Al alloy microstructures, each subjected to normal (i.e., null obliquity) penetration by an iron cylindrical projectile at an impact velocity V_I of either 1000 m/s or 1500 m/s. The dimensions of the projectile are diameter 20 mm and length 22 mm. The plate is 25.4 mm thick and 254 mm × 254 mm square in the lateral directions. These dimensions are sufficiently large to enable the projectile to penetrate completely through the target before interactions of the projectile with release waves from the lateral edges occur. Trends in results reported below are insensitive to refinement of the mesh via a ~ 50% increase in the number of elements.

The macroscopic models outlined in (21)–(26), with properties listed in Tables 2 and 3, are used for the plate and projectile. Properties for the Al plate are varied according to microstructure as listed in Tables 2 and 3: two textures each with three values of Ω provide a total of six property sets corresponding to six different microstructures. The EPIC dynamic finite element code [15] is used, in which elements are converted to interacting particles at large effective strains (> 0.5) to avoid numerical difficulties associated with severe mesh distortion [16,7]. In all simulations, the ductility of the aluminum plate is assigned a value of unity; when strained beyond this point, the deviatoric strength of the material degrades to zero locally. Library properties [15] for ductility and failure of the iron comprising the projectile are used in all 12 simulations.

Representative results in Fig. 4 depict the simulation after impact at 1500 m/s, with properties of the plate corresponding to random grain orientations and $\Omega = 1$. The plug that typically emerges in perforation of ductile plates impacted at high velocity [19,27] is evident in Fig. 4. Stress concentrations along the circumference of the perforated zone and symmetrically located in two other interior regions of the plate are evident, with magnitudes on the order of the maximum yield stress of the material (Fig. 2).

Shown in Fig. 5 is the ratio of the residual velocity V_R, i.e. the average steady-state velocity of the projectile (in the direction normal to the plate) after complete perforation, to the impact velocity V_I for all 12 simulations. The lower the value of V_R/V_I, the more resistant the plate to dynamic perforation. For each microstructure, this ratio decreases with decreasing impact velocity. Use of a cubic

Table 3
Parameters for dissipation fraction in coarse-scale model.

Parameter	Random texture			Cubic texture		
	$\Omega = 1$	$\Omega = 4$	$\Omega = 8$	$\Omega = 1$	$\Omega = 4$	$\Omega = 8$
B_1	−0.618	−2.457	−4.873	−0.673	−2.661	−5.224
B_2	0.861	3.478	7.054	1.025	4.101	8.176
B_3	−0.331	−1.350	−2.776	−0.415	−1.673	−3.378

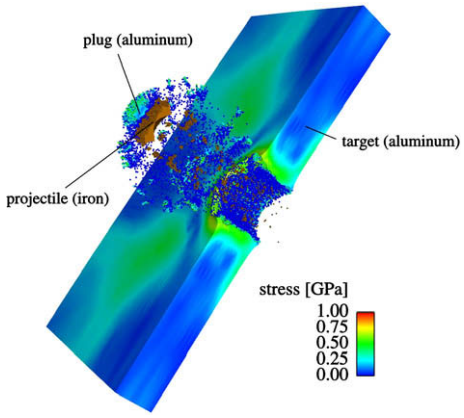

Fig. 4. Simulation of perforation of Al 2139 plate (random texture, $\Omega = 1$) by iron cylinder at initial velocity of 1500 m/s, shown here at 100 μs after initial impact. Effective stress contours in aluminum plate also shown.

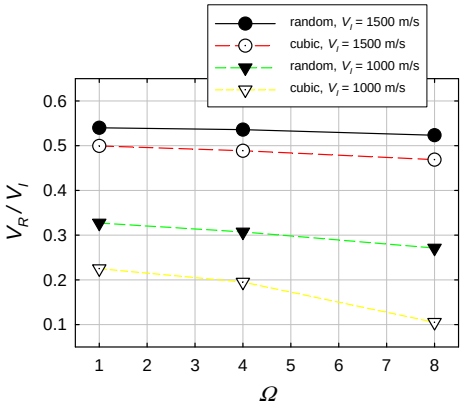

Fig. 5. Normalized residual velocity of projectile after perforation of Al plates with inelastic properties corresponding to various microstructures.

texture over a random texture seems to offer a ~10% reduction in V_R/V_I at an impact velocity of 1500 m/s and a 30% or greater reduction at an impact velocity of 1000 m/s. Recall however that the assumption of isotropy introduces some uncertainty into these predictions; a more thorough treatment would fit the polycrystal model results to an anisotropic yield surface [20]. Residual elastic energy storage in the plate also influences performance, with V_R/V_I reducing by ~5% as Ω is increased from 1 to 8 for an impact velocity of 1500 m/s, and V_R/V_I reducing by about ~20% as Ω is increased from 1 to 8 in the random microstructure at an impact velocity of 1000 m/s. The effect of stored elastic energy is even stronger for the cubic microstructure at an impact velocity of 1000 m/s, wherein V_R/V_I is reduced by over 50%, from 0.225 to 0.105, as Ω is increased from 1 to 8. The improvement in performance with increasing Ω occurs because as less adiabatic heating takes place in the penetration zone, less localized deformation results, delaying failure of the material.

6. Conclusions

A crystal plasticity model is developed for precipitate-hardened aluminum alloys accounting for large deformations, thermodynamics, nonlinear elasticity, and energy storage mechanisms and volume changes associated with residual stress fields of lattice defects. Direct numerical simulation of a polycrystalline microstructure with polygonal grains demonstrates variations from grain to

grain in stress fields due to anisotropy, as well as positive correlation of the heat dissipation fraction, adiabatic temperature rise, and plastic strain localization. A macroscopic plasticity model is calibrated to results of polycrystal simulations. The macroscopic model accounts, via choice of strain hardening parameters, for differences in shear strength afforded by texturing. The macroscopic model also captures effects of stored energy that depends on the strain history, and the model accounts for volume changes from defect generation in the equation of state for the hydrostatic pressure. Impact simulations demonstrate that improved resistance to ballistic perforation may be afforded by texturing to increase shear strength or by processing steps that increase the activity of dynamic energy storage mechanisms relative to dissipation mechanisms. In the future, in addition to shear localization, fracture should be given more consideration. For example, mesoscale simulations of the mechanism of spall fracture [33] that may occur in blast loading may provide insight into effects of statistical variability of microstructures, e.g. heterogeneous spatial distributions of grains and inclusions, on resistance to failure.

Acknowledgements

This work was supported by ARL WMRD and JIEDDO.

References

[1] Abu Al-Rub RK, Voyiadjis GZ. A direct finite element implementation of the gradient plasticity theory. Int J Numer Meth Eng 2005;63:603–29.
[2] Brown LM, Stobbs WM. Work hardening of copper-silica. 2. Role of plastic relaxation. Phil Mag 1971;23:1201–33.
[3] Cho A, Bes B. Damage tolerance capability of an Al–Cu–Mg–Ag alloy (2139). Mater Sci Forum 2006:603–8.
[4] Clayton JD. Dynamic plasticity and fracture in high density polycrystals: constitutive modeling and numerical simulation. J Mech Phys Solids 2005;53:261–301.
[5] Clayton JD. Modeling dynamic plasticity and spall fracture in high density polycrystalline alloys. Int J Solids Struct 2005;42:4613–40.
[6] Clayton JD. Two-scale modeling of effects of microstructure and thermomechanical properties on the dynamic performance of an aluminum alloy. Int J Mater Struct Integr, in press.
[7] Clayton JD. A model for deformation and fragmentation in crushable brittle solids. Int J Impact Eng 2008;35:269–89.
[8] Clayton JD, McDowell DL. A multiscale multiplicative decomposition for elastoplasticity of polycrystals. Int J Plasticity 2003;19:1401–44.
[9] Dwivedi SK, Asay JR, Gupta YM. Two-dimensional mesoscale simulations of quasielastic reloading and unloading in shock compressed aluminum. J Appl Phys 2006;100:083509.
[10] Farren WS, Taylor GI. The heat developed during plastic extension of metals. Proc R Soc Lond A 1925;107:422–51.
[11] Havner KS. Finite plastic deformation of crystalline solids. Cambridge: Cambridge University Press; 1992.
[12] Holder J, Granato AV. Thermodynamic properties of solids containing defects. Phys Rev 1969;182:729–41.
[13] Hull D, Bacon DJ. Introduction to dislocations. third ed. Oxford: Butterworth-Heinemann; 1984.
[14] Hutchinson CR, Fan X, Pennycook SJ, Shiflet GJ. On the origin of the high coarsening resistance of Ω plates in Al–Cu–Mg–Ag alloys. Acta Mater 2001;49:2827–41.
[15] Johnson GR, Stryk RA, Holmquist TJ, Beissel SR. Numerical algorithms in a Lagrangian hydrocode. AFWL-TR-1997-7039. Eglin AFB, FL: 1997.
[16] Johnson GR, Beissel SR, Stryk RA. A generalized particle algorithm for high velocity impact calculations. Comput Mech 2000;25:245–56.
[17] Kocks UF, Argon AS, Ashby MF. Thermodynamics and kinetics of slip. Prog Mater Sci 1975;19:1–288.
[18] Kohn BJ. Compilation of Hugoniot equations of state. AFWL-TR-1969-38. Kirtland AFB, NM: 1969.
[19] Li KZ, Goldsmith W. A phenomenological model for perforation of moderately thick plates by tumbling projectiles. Int J Solids Struct 1996;33:3561–75.
[20] Maudlin PJ, Schiferl SK. Computational anisotropic plasticity for high-rate forming applications. Comp Meth Appl Mech Eng 1996;131:1–30.
[21] Peirce D, Asaro RJ, Needleman A. An analysis of nonuniform and localized deformation in ductile single crystals. Acta Metall 1982;30:1087–119.
[22] Povrik GL, Mohan R, Brown SB. Crystal plasticity simulations of thermal stresses in thin-film aluminum interconnects. J Appl Phys 1995;77:598–606.
[23] Regueiro RA, Bammann DJ, Marin EB, Garikipati K. A nonlocal phenomenological anisotropic finite deformation plasticity model accounting for dislocation defects. ASME J Eng Mater Tech 2002;124:380–7.
[24] Rezvanian O, Zikry MA, Rajendran AM. Microstructural modeling of grain subdivision and large strain inhomogeneous deformation modes in f.c.c crystalline materials. Mech Mater 2006;38:1159–69.
[25] Rezvanian O, Zikry MA, Rajendran AM. Statistically stored, geometrically necessary and grain boundary dislocation densities: microstructural representation and modelling. Proc R Soc A 2007;463:2833–53.
[26] Rosakis P, Rosakis AJ, Ravichandran G, Hodowany J. A thermodynamic internal variable model for the partition of plastic work into heat and stored energy in metals. J Mech Phys Solids 2000;48:581–607.
[27] Schoenfeld SE, Kad BK. Texture effects on shear response in Ti–6Al–4V plates. Int J Plasticity 2002;18:461–86.
[28] Seeger A, Haasen P. Density changes of crystals containing dislocations. Phil Mag 1958;3:470–5.
[29] Taylor GI. The mechanism of plastic deformation of crystals. Proc R Soc Lond A 1934;145:362–415.
[30] Taylor GI. Plastic strain in metals. J Inst Metals 1938;62:307–24.
[31] Taylor GI, Quinney H. The latent energy remaining in a metal after cold working. Proc R Soc Lond A 1934;143:307–26.
[32] Thomas JF. Third-order elastic constants of aluminum. Phys Rev 1968;175:955–62.
[33] Vogler TJ, Clayton JD. Heterogeneous deformation and spall of an extruded tungsten alloy: plate impact experiments and crystal plasticity modeling. J Mech Phys Solids 2008;56:297–335.
[34] Wenk H-R, Van Houtte P. Texture and anisotropy. Rep Prog Phys 2004;67:1367–428.
[35] Wright TW. Stored energy and plastic volume change. Mech Mater 1982;1:185–7.
[36] Wright TW. The physics and mathematics of adiabatic shear bands. Cambridge: Cambridge University Press; 2002.
[37] Zerilli FJ, Armstrong RW. Dislocation–mechanics-based constitutive relations for material dynamics calculations. J Appl Phys 1987;61:1816–25.
[38] Zhou M, Clifton RJ, Needleman A. Finite element simulations of shear localization in plate impact. J Mech Phys Solids 1994;42:423–58.

NO. OF COPIES	ORGANIZATION
1 (PDF only)	DEFENSE TECHNICAL INFORMATION CTR DTIC OCA 8725 JOHN J KINGMAN RD STE 0944 FORT BELVOIR VA 22060-6218
1	DIRECTOR US ARMY RESEARCH LAB IMNE ALC HRR 2800 POWDER MILL RD ADELPHI MD 20783-1197
1	DIRECTOR US ARMY RESEARCH LAB RDRL CIM L 2800 POWDER MILL RD ADELPHI MD 20783-1197
1	DIRECTOR US ARMY RESEARCH LAB RDRL CIM P 2800 POWDER MILL RD ADELPHI MD 20783-1197
	ABERDEEN PROVING GROUND
1	DIR USARL RDRL CIM G (BLDG 4600)

NO. OF COPIES ORGANIZATION

1 DIRECTOR
US ARMY RESEARCH LAB
RDRL CI
R NAMBURU
2800 POWDER MILL RD
ADELPHI MD 20783-1197

ABERDEEN PROVING GROUND

44 DIR USARL
RDRL CIH C
P CHUNG
D GROVE
J KNAP
RDRL SL
R COATES
RDRL WM
B FORCH
S KARNA
J MCCAULEY
RDRL WMS
T JONES
RDRL WMM A
J ANDZELM
W NOTHWANG
RDRL WMM D
B CHEESEMAN
G GAZONAS
RDRL WMT A
R DONEY
S SCHOENFELD
RDRL WMT C
T BJERKE
T FARRAND
M FERMEN-COKER
S SEGLETES
B SCHUSTER
A TANK
W WALTERS
C WILLIAMS
RDR WMT D
S BILYK
D CASEM
J CLAYTON (10 CPS)
D DANDEKAR
N GNIAZDOWSKI
M GREENFIELD
Y HUANG
R KRAFT
B LOVE

NO. OF COPIES ORGANIZATION

M RAFTENBERG
E RAPACKI
M SCHEIDLER
T WEERASOORIYA